2011 IEEE International Conference on Robotics and Automation
Shanghai International Conference Center
May 9-13, 2011, Shanghai, China

Caging Micromanipulation for Automated Microassembly

David J. Cappelleri, Michael Fatovic, and Utsav Shah

Abstract— **This paper introduces the concept of caging micromanipulation for use in automated open loop microassembly tasks. Utilizing a caging transport motion primitive along with rotational and translation primitives, we demonstrate full control of the state of the part. Additionally, a framework for planar microassembly task planning is provided based on the A* algorithm. It is used to determine the optimal assembly sequences and part starting locations in the workspace. We also describe a test-bed suitable for planar micro, meso-scale, and nano-scale manipulation and assembly tasks and present simulation and experimental results of this work.**

I. INTRODUCTION

Gripping and manipulation techniques for micro-assembly applications is an active area of research [1]. Specifically, there is a body of work pertaining to pick-and-place micro-assembly tasks using micro-gripping techniques and strategies [2], [3], [4], [5], [6], [7], [8]. For micro-scale manipulation, sticking effects due to Van der Walls forces and static electricity make the manipulator motions and part release complicated [9], [10]. Micro-manipulators also have limited degrees of freedom when compared to manipulators at the macro-scale. Some of these problems are addressed in [11]. However, the focus here is rather on using micro-scale pushing operations, which are better suited for open loop or quasi-open loop manipulations, for solving a representative microassembly problem as shown in Fig. 1.

The derivation of the fundamental mechanics of pushing operations and sliding objects have been extensively studied by [12], [13], [14]. There is also extensive work addressing the analysis and simulation of mechanical systems with frictional contacts [15], [16]. In particular, the problem of finding motion primitives that rely on pushing and are robust to errors has received significant attention [17], [18], [19].

Much work has been done on investigating techniques and strategies for micromanipulation (see review in [20]). However, literature addressing micromanipulation with real-time sensor feedback is limited. The primary reason for this is that obtaining accurate sensor data is a difficult problem at this scale. Sensors cannot easily be affixed to tiny precision instruments without compromising their functionality [10]. The use of high resolution optical systems with controllable parameters for micro-assembly tasks are examined by [21]. Even with this sensor data, calibration and vision-based control at this scale can present technical difficulties. Without accurate sensor data, it is hard to develop models, and therefore controllers, for micromanipulation.

Previous work on cooperative manipulation has utilized the concepts of form and force closure to manipulate large objects [22], [23], [24]. The force closure condition assumes that the grasp on the object can withstand any external force applied to the object. Form closure can be defined as the condition to guarantee force closure without requiring frictional contacts to do so [25]. It is possible to use conditional force closure to transport an object by pushing on it from an initial position to a goal position [26], [19]. Conditional force closure makes use of both the manipulation forces generated by contacts from the robots as well as the external forces acting on the object, such as friction and gravity. Object closure or caging is variation of this. It simply requires that the objected be caged by the robots and confined to a compact set in the configuration space [27]. In [28], decentralized control policies for a group of mobile robots to move toward a goal position while maintaining the object closure condition are presented. Multirobot manipulation of non-circular objects and cooperative manipulation in environments with obstacles has recently been demonstrated [29], [27] with macro-scale mobile robots. We look to use similar principles here for micromanipulation and assembly tasks. While a multi-fingered micromechanism for coordinated micro/nano manipulation has been presented in [30], it has a very limited range of motion and is not well-suited for high throughput assembly of micro-scale components and devices. We build on our prior work [31], [32] and [33] to construct rotational and 1D translation motion primitives and develop a new micro-scale caging transport primitive here. We also present a planning and search algorithm to identify an optimal part starting location for a particular micro-assembly sequence as well as for determining the optimal assembly sequence for a give part starting location along with simulation and experimental results.

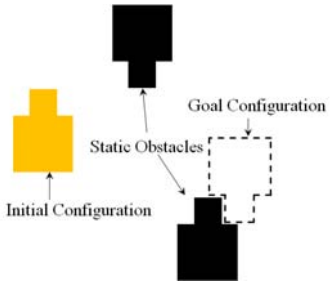

Fig. 1. Representative microassembly problem

II. PROBLEM FORMULATION

We consider a group of N micromanipulators with single point probes (robots) operating in the XY plane with kinematics given by

$$\dot{q}_{m_i} = u_{m_i} \tag{1}$$

where $q_{m_i} = (x_{m_i}, y_{m_i})^T$ and u_{m_i} denote the i^{th} tip position of the manipulator's probe and corresponding control input. We assume each manipulator is localized in a global coordinate frame. Our objective is to design a set of control inputs to enable a team of N micromanipulators to surround and transport an object to a desired location and orientation while avoiding obstacles in the environment in order to solve the representative microassembly problem depicted in Fig.1.

D. Cappelleri, M. Fatovic, and U. Shah are with the Multi-Scale Robotics and Automation Lab, Department of Mechanical Engineering, Stevens Institute of Technology, 1 Castle Point on Hudson, Hoboken, NJ USA 07030 [dcappell, mfatovic, ushah1] @stevens.edu

III. METHODOLOGY

A. Assumptions

We follow the methodology presented in [27] and adapt it for our case. Assume a convex workspace $\mathcal{W}$ with a boundary denoted by $\partial\mathcal{W}$. Given a part whose centroid is denoted as (x_p, y_p), we assume there exists a smooth shape, $\mathcal{S}$, whose boundary, $\partial\mathcal{S}$, is a smooth, regular, closed curve with the form $s(x, y) = 0$ such that the part is contained within $\partial\mathcal{S}$. The shape $\mathcal{S}$ can always be found by considering two parameters (shown in Fig. 3(a)) for the part of interest: (1) D_{min}: the smallest gap through which the part will fit and (2) D_{max}: the maximum distance between any two points on the part. Therefore, for any given part, the circular boundary with radius:

$$r_{cage} = (1/2)D_{max} + \epsilon \tag{2}$$

where $\epsilon > 0$ is a constant scalar, will always contain the object. This is referred to as the *caging* circle. For a given r_{cage} and D_{min}, there must be at least $N_{min} > 0$ number of manipulators (robots) to ensure object closure. Thus we make the following assumptions and let $d(\cdot, \cdot)$ denote the Euclidean distance between any two positions in $\mathcal{W}$:

1) $N_{min} \leq N \leq N_{max}$
2) $d_{max}(q_p, q_{m_i}) \leq r_{cage}$ for i = 1, ..., *N* in the *Transport* mode
3) $d_{min}(q^o_{obstacle}, \partial\mathcal{W}) > r_{cage} + \epsilon$, where $q^o_{obstacle}$ is the initial position of the obstacle
4) $d_{min}(q^o_{obstacle}, q_{m_i}) \geq r_{cage}$ for all *k* obstacles in $\mathcal{W}$
5) $d_{min}(q_{obstacle}, q_{m_i}) \geq D_{max}/2$ in order to enter *Rotation* mode

Assumption 1 ensures that the manipulators will be able to surround the object and achieve closure. Assumption 2 ensures that the manipulators will be able to maintain closure when transporting the part throughout the workspace. Assumption 3 and 4 ensure that the part is initially located at a position where the robots can surround it without colliding with the workspace boundary or other obstacles in the environment while Assumption 5 ensures a collision free region for part rotations to be performed.

B. Approach

Our approach to microassembly consists of the manipulation plans consisting of three types of micromanipulation techniques to robustly control the position and orientation of the part of interest. Three types or modes of operation are utilized: *Caging Transport*, *Rotation*, and *One-Sided Pushing Translation*. The manipulation plans we generate call for caging manipulation to transport the part from it's initial location to an orthogonal location $\geq D_{max}$ away from the goal location, while avoiding obstacles. A rotation primitive follows to orientate the part to the final goal orientation. Finally, a short one-sided pushing (OSP) X or Y translation primitive is executed to position the part into it's final goal location in the assembly.

1) Caging Transport: When using caging micromanipulation for transporting the part of interest, we assume that if object closure is maintained, the part's centroid, (x_p, y_p), will always lie within the caging circle. Guarantees of part rotation are not made but they can be limited by utilizing tighter caging parameters driven by the part geometries, which will be described later. The microrobotics test-bed used here (Fig.6) allows for use of up to *N* = 4 manipulators

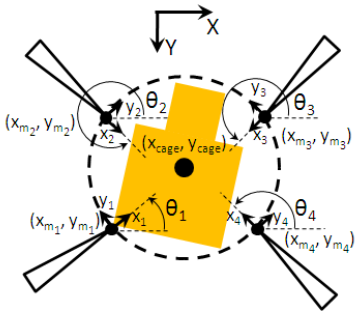

Fig. 2. Caging circle defined by four micromanipulators

for micro-scale caging transport operations, as seen in Fig.2. The manipulator tips are restricted to not cross the caging circle. For a given r_{cage} and D_{min}, the minimum number of manipulators needed to achieve object closure is

$$N_{min} = 2\pi r_{cage}/D_{min} \tag{3}$$

To translate the center position of the cage, (x_{cage}, y_{cage}), we must map the control inputs, $U_{cage} = [u_{x_{cage}} u_{y_{cage}} 0]^T$, to the local frames of the micromanipulators being utilized. Each manipulator control input, u_{m_i}, must be prescribed in the local coordinate frame orthogonal to the manipulator's orientation (θ_i, i = 1,..,4, as defined in Fig. 2) and are given by

$$u_{m_i} = T_i U_{cage} = \begin{bmatrix} u_{x_{m_i}} \\ u_{y_{m_i}} \\ u_{z_{m_i}} \end{bmatrix} \tag{4}$$

where T_i corresponds to the transformation matrix for each manipulator listed in equations (5)-(8). These equations allow for the desired position of the cage to drive the movement of the manipulators and provides a robust transport motion primitive, as shown in Fig.3(a).

$$T_1 = R_x(180^\circ)R_z(\theta_1) = \begin{bmatrix} cos(\theta_1) & -sin(\theta_1) & 0 \\ -sin(\theta_1) & -cos(\theta_1) & 0 \\ 0 & 0 & -1 \end{bmatrix} \tag{5}$$

$$T_2 = R_x(180^\circ)R_z(\theta_2) = \begin{bmatrix} cos(\theta_2) & -sin(\theta_2) & 0 \\ -sin(\theta_2) & -cos(\theta_2) & 0 \\ 0 & 0 & -1 \end{bmatrix} \tag{6}$$

$$T_3 = R_z(\theta_3) = \begin{bmatrix} cos(\theta_3) & -sin(\theta_3) & 0 \\ sin(\theta_3) & cos(\theta_3) & 0 \\ 0 & 0 & 1 \end{bmatrix} \tag{7}$$

$$T_4 = R_z(\theta_4) = \begin{bmatrix} cos(\theta_4) & -sin(\theta_4) & 0 \\ sin(\theta_4) & cos(\theta_4) & 0 \\ 0 & 0 & 1 \end{bmatrix} \tag{8}$$

2) Rotation: The rotational motion primitive [32] for the polygonal part of interest is shown in Fig.3(b). It consists of one stationary manipulator probe and one active manipulator probe. They are positioned symmetrically above and below the center of mass of the part with a vertical separation distance, d_v, according to:

$$max(d_w, d_l) \geq d_v \geq min(d_w, d_l) \cdot (3/4) \tag{9}$$

where d_w and d_l are the length and width dimensions of the part, respectively. Once in position, the active probe is translated along the X-axis causing the part to pivot around the stationary probe's tip at the base of the part. Translating

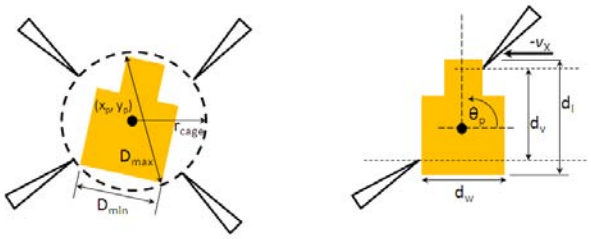

(a) Caging Transport Primitive (b) Rotation Primitive

Fig. 3. Caging Transport and Rotation Primitives

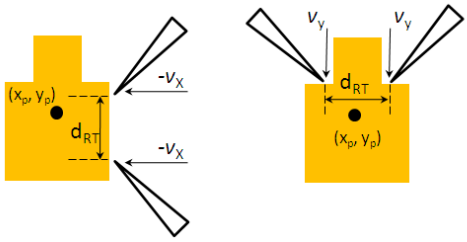

(a) OSP X Translation Primitive (b) OSP Y Translation Primitive

Fig. 4. One-sided Pushing X and Y Translation Primitives.

the active probe a distance greater than d_w will rotate the part $90°$.

3) One-Sided Pushing 1D Translation: Once the part is in it's final orientation a short orthogonal distance ($\simeq D_{max} + \epsilon$) from the goal position, a one-sided pushing (OSP) 1D translation either in the X or Y direction is needed to translate the part to the goal position in the assembly. The caging transport primitive cannot be used here since the manipulator probes surrounding the part in this case will interfere with the part mating with another part. OSP translation is performed using two manipulators forming a two-point sticking contact about the center of mass the part along one side to reliably control it's position. The separation distance for the OSP translation primitives, d_{RT}, is given by

$$d_{RT} = d_L(1/2) \tag{10}$$

where d_L is the length of the side of the part that is being pushed.

C. Planning & Search Algorithm

The general problem we are interested in solving is shown in Fig.5(a). We consider four different start positions (*SP 1 to SP 4*) for the part and four different assembly positions (*AP 1 to AP 4*). Mimicking a part feeder in industrial macro-scale operations, it is assumed that all the micro-scale parts utilized for a particular assembly start from one of the starting positions and the parts can be assembled into assembly positions in any sequence.

A dual path planning and search algorithm has been created based on the A* algorithm [34] to find optimal solutions to this problem. A collision free path for the part is produced that is the shortest path from it's starting position to the assembly position. For assemblies consisting of *n* parts, *n* successive iterations of the A* algorithm are employed. For the first part of the assembly, there is no obstacle in the workspace yet so the path achieved by the algorithm is a basic A* algorithm finding the shortest and optimum path in an obstacle free configuration space. However for the successive parts, the previous parts act as an obstacle when finding the new path: i.e. the first part acts as an obstacle for the next batch of parts in the assembly and the second part along with the first will act as obstacles for the remaining parts and so on. For these sequences, the algorithm finds the optimum shortest path while avoiding the obstacles. To ensure obstacle avoidance, collision detection for the entire caging circle encompassing the part is accounted for, rather than just the part geometry alone. The final step in path for the part is also restricted to an orthogonal move (X or Y translation) to avoid collision of the manipulators (when they are in a caging configuration) and other parts in the assembly. For the grid size used here, each A*-determined optimal path computes in approximately 200 seconds.

TABLE I

PLANNING & SEARCH ALGORITHM RESULTS

A. Optimal starting position search for a given assembly sequence

Start Position	Assembly Sequence	Assembly Length
SP 1	AP 1 - AP 2 - AP 3 - AP 4	1415
SP 2	AP 1 - AP 2 - AP 3 - AP 4	1048
SP 3	AP 1 - AP 2 - AP 3 - AP 4	1030
SP 4	AP 1 - AP 2 - AP 3 - AP 4	1268

B. Optimal assembly sequence search for a given starting location

Start Position	Assembly Sequence	Assembly Length
SP 1	AP 3 - AP 4 - AP 2 - AP 1	1284
SP 2	AP 3 - AP 4 - AP 1 - AP 2	932
SP 3	AP 1 - AP 2 - AP 4 - AP 3	900
SP 3	AP 1 - AP 4 - AP 2 - AP 3	900
SP 4	AP 2 - AP 1 - AP 3 - AP 4	1151

The assembly planning algorithm is also used to search for the optimal part starting position in the workspace for a particular known assembly sequence as well as for the opposite case of determining the optimal assembly sequence for a predetermined part starting location in the workspace. A brute-force search of all the possible assembly and sequences and starting locations is performed and the total path distance for all the parts is summed to yield an assembly length metric. The sequence or starting position with the shortest assembly length is denoted as the optimal assembly sequence or starting part position. Table I-A shows the simulation results for a given assembly sequence of {AP 1 - AP 2 - AP 3 - AP 4} with the various start positions for the parts. It is found that *SP 3* yields the shortest assembly length. The corresponding part paths for this start position and assembly sequence are shown in Fig.5(b)(top). Once the part is in the assembly position, it is shaded in the figure identifying it as an obstacle when finding a path for the next part. In Table I-B, the best assembly sequences that have been identified when all the parts starting from one particular starting position are listed. The optimal assembly sequence determined for *SP 1* are {AP 3 - AP 4 - AP 2 - AP 1} and the corresponding part paths for this start position and optimal assembly sequence are shown in Fig.5(b)(bottom). In the case of *SP 3*, two assembly sequences yielded the same shortest assembly length (900).

IV. EXPERIMENTAL RESULTS

A. Experimental Setup

The microrobotics test-bed used here (Fig.6) is well-suited for automated microrobotic manipulation and assembly experiments at the nano-, micro-, and meso-scales. The test-bed consists of an inverted optical microscope (Nikon Ti-U), automated XY stage with encoders (Nikon Ti-S-ER), CCD camera (QImaging Retigna 200R), and four computer-controlled manipulators (Sutter Instruments MPC-285) with

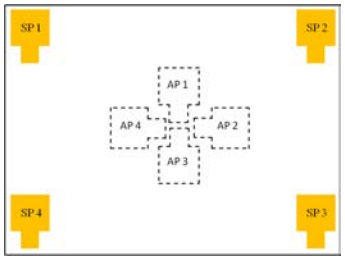

(a) Planning Problem Setup

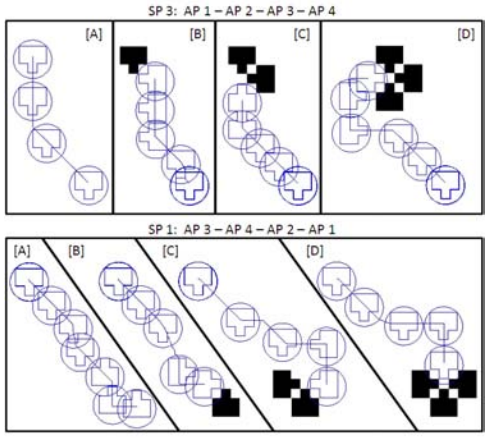

(b) Simulated Optimal Plans

Fig. 5. Problem Setup and Simulation Results

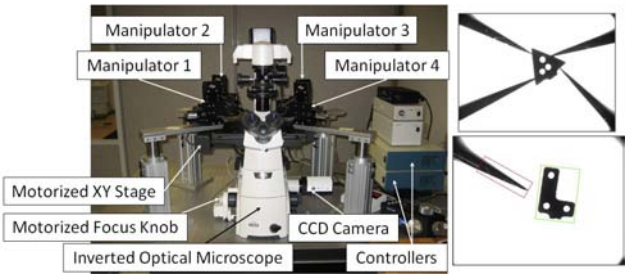

Fig. 6. Microrobotics Test-bed

3 controllable degrees-of-freedom with a minimum step size of 62.5 nm, and customized controllers. A custom LabView-based control program was development to allow for real-time vision position feedback and simultaneous control of all the manipulators and parts in the system. The manipulators are outfitted with tungsten probes with 25 μm diameter tips. Manipulation and assembly tests were performed on parts made from SU-8 resist (*www.microchem*) with $D_{min} = 580\mu$m and $D_{max} = 700\mu$m. The part thickness is 50 μm. A 4X objective was used in the microscope providing a field of view of approximately 3800 μm X 2850 μm. The camera images are 640 x 480 pixels in size, corresponding to resolution of about 10 μm/pixel. Using this test-bed, experimental manipulation tests for each motion primitive described were conducted as well as representative assembly task executed. These results will be described now.

B. Experimental Results - Motion Primitives

1) Caging Transport: Caging transport tests to manipulate the part along a square path of 500 μm, 1000 μm, and 1500 μm were performed. Following (2) and (3), r_{cage} was calculated to be 350 μm and the minimum number of

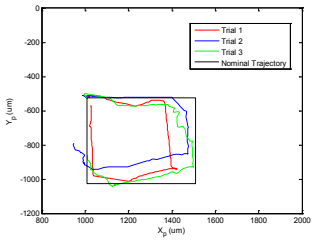

(a) x_p,y_p Trajectories - Original Cage

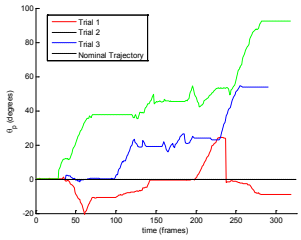

(b) θ_p Trajectories - Original Cage

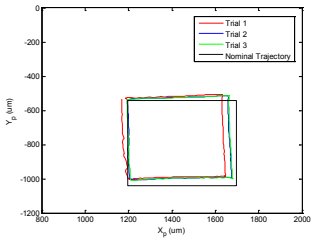

(c) x_p, y_p Trajectories - FD Cage

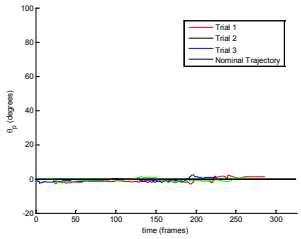

(d) θ_p Trajectories - FD Cage

Fig. 7. Caging Transport Primitive Part Trajectories

TABLE II
TRANSPORT, TRANSLATION AND ROTATION EXPERIMENTAL RESULTS

A. Part Transport Results with Original Caging Parameters

Transport Square Path Distance (μm)	Ave Max Error $x_p(\mu$m)	Ave Max Error $y_p(\mu$m)	Ave θ_p Change ($^\circ$)
500	111	229	64
1000	233	224	86
1500	290	290	77

B. Part Transport Results with Feature Defined Cage

Transport Square Path Distance (μm)	Ave Max Error $x_p(\mu$m)	Ave Max Error $y_p(\mu$m)	Ave θ Change ($^\circ$)
500	45	48	4
1000	103	83	11
1500	143	120	9

C. Part OSP X and Y-direction Translation Results

Translation Distance (μm)	Ave Max Error $x_p(\mu$m)	Ave Max Error $y_p(\mu$m)	Ave θ Change ($^\circ$)
X-dir: 500	21	33	4
X-dir: 1000	83	34	24
Y-dir: 500	5	35	3
Y-dir: 1000	19	56	3

D. Part Rotation Results

Rotation Angle ($^\circ$)	Ave X and Y Change $x_p(\mu$m)	Ave X and Y Change $y_p(\mu$m)	Ave θ Error ($^\circ$)
90	152	36	9

manipulators needed to create the cage was calculated as N_{min} = 4. The part x_p, y_p and θ_p trajectories for the 500 μm square path tests when using these caging parameters are shown in Fig. 7(a) and Fig. 7(b), respectively. At least three trials for each transport test were conducted and the average maximum error for x_p and y_p were compiled along with the average change in the θ_p for each set of tests. This data is shown in Table II-A. While the center of mass of the part does remain inside the caging circle boundary during the duration of the tests, there is quite a bit of movement of the part within the cage. This is evidenced by the large x_p and y_p error values in the table, corresponding to about 20% of the path distance for each transport test, and large change in θ_p values. It is also obvious when observing the part trajectories and change in θ_p plots in comparison to

the nominal trajectories and angle change in Fig.7(a) and Fig.7(b). This is because in the original formulation [27] for defining the r_{cage} and N_{min} values, circular robots with a finite radius are used. In our case, point robots (manipulator probes) are being used instead. Larger size robots (end-effectors) would provide more contact area with and protrude into the cage, essentially limiting the free space in the cage that the part can move during the transport primitive. This, along with the fact that we are manipulating objects at the micro-scale with small assembly tolerances, requires a tighter cage to be used for robust transport of the micro-scale part. Thus, we use the part features to define the positions for the probe tips. Two probes are positioned inside the two concave features of the part an ϵ distance away from the part, similar to the probes shown in Fig. 4(b), while the other two probes are positioned opposite them, along the bottom edge of the part also an ϵ distance away. This grasp is similar to a form closure grasp but relaxed enough to be considered a cage and we refer to it as a *feature defined (FD) cage*. Table II-B summarizes the transport manipulation test results conducted using the FD cage for 500, 1000, and 1500 μm square path tests. The average maximum error values for the part's position and average orientation change values have been greatly reduced, i.e.: only systematic errors of about 10% of the transport distance and orientation changes of only a few degrees. Figs.7(c) and 7(d) show the trajectory plots for the 500 μm square path transport test. These trajectories are much smoother and consistent over all the trials, while the part orientation changes only slightly.

2) Rotation: At least three trials for part rotation tests were performed as illustrated in Fig. 3(b). For our part, d_w = d_l = 580 μm and d_v was set to 435 μm. TableII-D lists the average of the experimental trials for a desired part rotation of 90°. The average error θ_p is only 9°. There are some changes in the x_p and y_p position of the part, which is expected, but small. They can be mitigated with a robust translation move following the part rotation, if needed.

3) OSP 1D Translation: At least three trials for both the OSP X- and Y-direction translation tests were performed as shown in Fig. 4 with d_{RT} = 290 μm. The average maximum error for x_p, y_p and the average change in θ_p calculated and are shown in Table II-C. Translation tests for distances of both 500 and 1000 μm in each direction were done. The errors are small in all cases, accurate to within our part tracking algorithm uncertainty: $\pm$ 1 pixel = $\pm$ 10 μm.

C. Experimental Results - Microassembly Task

Experimental trials for the planned path of last step in the optimal assembly sequence for start location *SP 1* (Fig.5(b)(top - Step D) were executed in the test-bed. Two types of primitives are utilized - caging transport and a one-sided pushing Y-translation - and carried out in open loop. The trajectories of the part's position (x_p and y_p) and orientation (θ_p) for three trials are shown in Figs. 8(a) and 8(b) (Note: Frame rate is about 15 frames/sec). From the results of the square path tests for the featured defined caging transport primitive, we can see a systematic error of approximately 10% of the transport distance. Noting this, the initial start position of the part in the experiments was offset 10% of the of the overall caging transport distances along the X- and Y-axis, respectively. Microscope field of view images showing the part being assembled are pictured in Fig. 8(c). The plots in Figs. 8(a) is annotated to show correspondence to the relevant image in Fig. 8(c). Note:

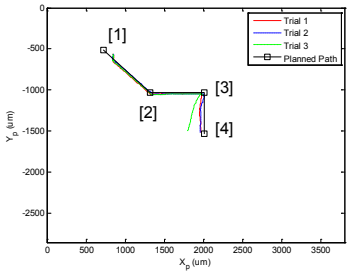

(a) x_p and y_p Trajectories

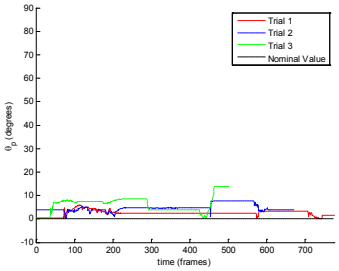

(b) θ_p Trajectories

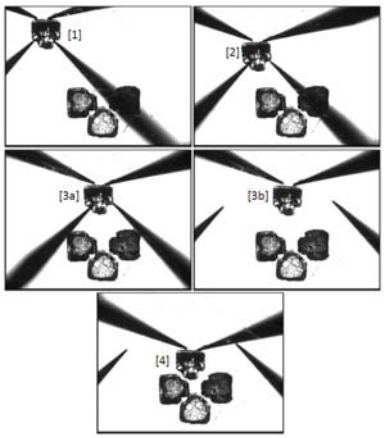

(c) Microscope field of view images during part assembly

Fig. 8. Microassembly Test Results

Fig. 8(c)[3a] shows the part after the completion of the caging transport primitive, while [3b] shows the part in the same position, after the manipulators have been reconfigured, at the start of the one-sided pushing Y-translation primitive. Two of three trials successfully manipulated the part to its goal assembly position in the appropriate orientation. In trial 3, the OSP Y-translation resulted in some X-axis translation as well, causing the assembly to fail. This was due to off-center positioning of the probe tips during at start of the push resulting in only a point sticking contact of one of the probes and subsequent diagonal part translation.

The starting orientation for the part was rotated 90° in order to evaluate a manipulation plan that requires all three of the motion primitive described here. Microscope field of view images during the execution of the plan for one trial are shown in Fig. 9. The part positions in Fig. 9[1], [2], and [3] are the same as the ones shown in Fig. 8(c)[1], [2], and [3] and are accomplished with the caging transport primitive. Once the part is in position [3], the rotational primitive is executed. Fig. 9 shows the part in position [3] at the end of the transport primitive [3a], at the start [3b] and end [3c] of the rotational primitive, and with the manipulator probes positioned for the start of the OSP Y-translation [3d]. Fig. 9[4] and [5] show the part successfully translating in the Y-direction to it's goal assembly position. While this trial worked, in other trials the coupled translation of part when performing the rotation primitive caused the assembly to fail when following the *a priori* planned path. Rather than execute the manipulation and assembly plan entirely open loop, it would be helpful to consider a quasi-open loop type of control scheme to check the state of the part after each primitive and re-plan accordingly to increase the success rate.

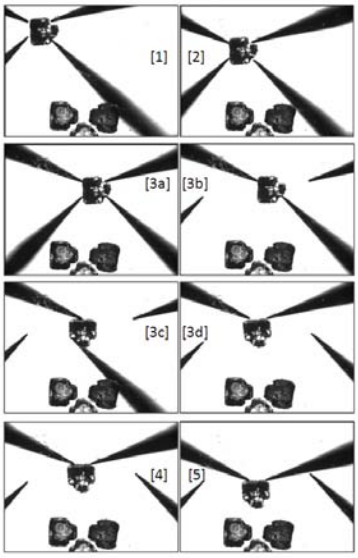

Fig. 9. Microassebly test result requiring the use of all three primitives

Also, the order of the motion primitives could be examined. For example, executing the rotational primitive first and then re-planning the path from that position of the part in it's proper orientation is expected to yield the same results as those presented in Fig. 8 where the part starts in it's goal orientation at the start.

V. CONCLUSIONS

In this paper, we have demonstrated a new caging transport motion primitive for micromanipulation and microassembly tasks. It can be used in conjunction with rotational and 1D translation motion primitive to yield complete control over the state of the part in open loop microassemby task planning and execution. We have also presented a dual path planning and search algorithm to identify the optimal part and starting location (bin) in the workspace for a predefined assembly sequence along with the optimal assembly sequence and path for a given part starting location. Experimental results of open loop execution of a sample plan generated show the potential for using this methodology for fully automated microassembly tasks with greater complexity.

REFERENCES

[1] J. Cecil, D. Vasquez, and D. Powell, "A review of gripping and manipulation techniques for micro-assembly applications," International Journal of Production Research, vol. 43, no. 4, pp. 819–828, February 2005.

[2] J. Feddema, P. Xavier, and R. Brown, "Micro-assembly planning with van der Waals force," Proceedings of the IEEE International Symposium on Assembly and Task Planning (ISATP '99), pp. 32 –38, July 1999.

[3] Y. Zhou and B. Nelson, "The effect of material properties and gripping force on micrograsping," in Proceedings of the IEEE International Conference on Robotics & Automation (ICRA), San Francisco, CA, April 2000.

[4] C. Keller, "Microgrippers with integrated actuator and force sensors," in Proceedings of the World Automation Congress, 1998, pp. 217–222.

[5] J. Cecil and N. Gobinath, "Development of a virtual and physical cell to assemble micro devices," Special Issue of the Journal of Robotics and CIM, pp. 431–441, August-October 2005.

[6] J. Alex, B. Vikramaditya, and B. Nelson, "A virtual reality teleoperator interface for assembly of hybrid MEMS prototypes," Proceedings of DETC98 1998 ASME Engineering Technical Conference, Atlanta, GA, Sept. 13-16 1998.

[7] T. Kasaya, H. Miyazaki, S. Saito, and T. Sato, "Micro object handling under SEM by vision-based automatic control," Proceedings of the IEEE International conference on Robotics and Automation, Detroit, MI, pp. 2189–2196, 1999.

[8] A. Das, P. Zhang, W. Lee, D. Popa, and H. Stephanou, "μ^3: Multiscale, deterministic micro-nano assembly system for construction of on-wafer microrobots," in IEEE International Conference on Robotics and Automation (ICRA), Rome, Italy, April 2007.

[9] R. Fearing, "Survey of sticking effects for micro parts handling," IEEE/RSJ Int. Conf. on Intelligent Robotics and Sys.(IROS), Pittsburgh, PA, vol. 2, pp. 212–217, August 5-9 1995.

[10] K. Boehringer, R.Fearing, and K. Goldberg, Handbook of Industrial Robotics, 2nd Ed. John Wiley and Sons, 1999, ch. Microassembly, pp. 1045–1066.

[11] M. Moll, K. Goldberg, M. Erdmann, and R. Fearing, "Orienting micro-scale parts with squeeze and roll primitives," IEEE Int. Conf. on Robotics and Automation, Washington, DC, May 11-15 2002.

[12] M. Mason, "Manipulator grasping and pushing operations," Ph.D. dissertation, Massachusetts Institute of Technology, 1982.

[13] ——, "Mechanics and planning of manipulator pushing operations," International Journal of Robotics Research, vol. 5, no. 3, pp. 53–71, 1986.

[14] M. Peshkin and A. Sanderson, "The motion of a pushed, sliding object, Part 1: Sliding friction," Robotics Institute, Carnegie Mellon University, Pittsburgh, PA, Tech. Rep. CMU-RI-TR-85-18, September 1985.

[15] P. Song, J. Pang, and V. Kumar, "A semi-implicit time-stepping model for frictional compliant contact problems," International Journal for Numerical Methods in Engineering, Accepted for publication 2004.

[16] J. Trinkle, S. Berard, and J. Pang, "A time-stepping scheme for quasistatic multibody systems," International Symposium of Assembly and Task Planning, July 2005.

[17] M. Salganicoff, G. Metta, A. Oddera, and G. Sandini, "A vision-based learning method for pushing manipulation," AAAI Fall Symp. on Machine Learning in Computer Vision., 1993b.

[18] Z. Balorda, "Reducing uncertainty of objects by robot pushing," IEEE Int. Conf. on Robotics and Automation, pp. 1051–1056, 1990.

[19] K. Lynch and M. Mason, "Stable pushing: Mechanics, controllability, and planning," International Journal of Robotics Research, vol. 15, no. 6, pp. 553–556, December 1996.

[20] M. Savia and H. Koivo, "Contact micromanipulation-survey of strategies," Mechatronics, IEEE/ASME Transactions on, vol. 14, no. 4, pp. 504–514, Aug. 2009.

[21] B. Vikramaditya and B. Nelson, "Visually guided microassembly using optical microscopes and active vision techniques," IEEE Int. Conf. on Robotics and Automation, Albuquerque, New Mexico, 1997.

[22] K. Kosuge, Y. Hirata, H. Kaetsu, and K. Kawabata, "Motion control of multiple autonomous mobile robots handling a large object in coordination," IEEE Int. Conf. on Robotics and Automation, pp. 2666–2673, May 1999.

[23] D. Rus, "Coordinated manipulation of objects in a plane," Algorithmica, vol. 19, no. 1, pp. 129–147, 1997.

[24] T. Sugar and V. Kumar, "Multiple cooperating mobile manipulators," IEEE Int. Conf. on Robotics and Automation, pp. 1538–1543, 1999.

[25] J. Salisbury and B. Roth, "Kinematic and force analysis of articulated hands," ASME Journal of Mechanisms, Transmissions, and Automation in Design, vol. 104, no. 1, pp. 33–41, 1982.

[26] M. Mataric, M. Nilsson, and K. Simsarian, "Cooperative multi-robot box-pushing," IEEE/RSJ Int. Conf. on Intelligent Robots and Systems, pp. 556–561, 1995.

[27] J. Fink, M. A. Hsieh, and V. Kumar, "Multi-robot manipulation via caging in environments with obstacles," in 2008 IEEE International Conference on Robotics and Automation, Pasedena, CA, May 2008.

[28] G. Pereira, V. Kumar, and M. Campos, "Decentralized algorithms for multi-robot manipulation via caging," The Int. Journal of Robotics Research, vol. 23, no. 7/8, pp. 783–795, 2004.

[29] N. M. J. Fink and V. Kumar, "Composition of vector fields for multi-robot manipulation via caging," Robotics: Science and Systems III, 2007.

[30] S. Krishnan and L. Saggere, "A multi-fingered micromechanism for coordinated micro/nano manipulation," J. Micromech. Microeng., vol. 17, pp. 576–585, 2007.

[31] D. Cappelleri, J. Fink, B. Mukundakrishnan, V. Kumar, and J. Trinkle, "Designing open-loop plans for planar micro-manipulation," IEEE Int. Conf. on Robotics and Automation, Orlando, FL, May 2006.

[32] P. Cheng, D. Cappelleri, B. Gavrea, and V. Kumar, "Planning and control of meso-scale manipulation tasks with uncertainties," in Proceedings of Robotics: Science and Systems, Atlanta, GA, USA, June 2007.

[33] V. K. Peng Cheng, Jonathan Fink, "Abstractions and algorithms for cooperative multiple robot planar manipulation," in Proceedings of Robotics: Science and Systems IV, Zurich, Switzerland, June 2008.

[34] H. Choset, W. Burgard, S. Hutchinson, G. Kantor, L. E. Kavraki, K. Lynch, and S. Thrun, Principles of Robot Motion: Theory, Algorithms, and Implementation. MIT Press, April 2005.